pH-Controlled Gas-Generating Mineralized Nanoparticles: A Theranostic Agent for Ultrasound Imaging and Therapy of Cancers

Kyung Hyun Min,[†,‡] Hyun Su Min,[†] Hong Jae Lee,[§] Dong Jin Park,[∥] Ji Young Yhee,[†] Kwangmeyung Kim,[†] Ick Chan Kwon,[*,†] Seo Young Jeong,[∥] Oscar F. Silvestre,[‡] Xiaoyuan Chen,[‡] Yu-Shik Hwang,[§] Eun-Cheol Kim,[⊥] and Sang Cheon Lee[*,§]

[†]Center for Theragnosis, Biomedical Research Institute, Korea Institute of Science and Technology, Seoul 136-791, Republic of Korea, [‡]Laboratory of Molecular Imaging and Nanomedicine (LOMIN), National Institute of Biomedical Imaging and Bioengineering (NIBIB), National Institutes of Health (NIH), Bethesda, Maryland 20892, United States, [§]Department of Maxillofacial Biomedical Engineering & Institute of Oral Biology, School of Dentistry, Kyung Hee University, Seoul 130-701, Republic of Korea, [∥]Department of Life and Nanopharmaceutical Science, College of Pharmacy, Kyung Hee University, Seoul 130-701, Republic of Korea, and [⊥]Department of Maxillofacial Tissue Regeneration and Research Center for Tooth and Periodontal Regeneration (MRC), School of Dentistry, Kyung Hee University, Seoul 130-701, Republic of Korea

ABSTRACT We report a theranostic nanoparticle that can express ultrasound (US) imaging and simultaneous therapeutic functions for cancer treatment. We developed doxorubicin-loaded calcium carbonate ($CaCO_3$) hybrid nanoparticles (DOX-$CaCO_3$-MNPs) through a block copolymer templated *in situ* mineralization approach. The nanoparticles exhibited strong echogenic signals at tumoral acid pH by producing carbon dioxide (CO_2) bubbles and showed excellent echo persistence. *In vivo* results demonstrated that the DOX-$CaCO_3$-MNPs generated CO_2 bubbles at tumor tissues sufficient for echogenic reflectivity under a US field. In contrast, the DOX-$CaCO_3$-MNPs located in the liver or tumor-free subcutaneous area did not generate the CO_2 bubbles necessary for US contrast. The DOX-$CaCO_3$-MNPs could also trigger the DOX release simultaneously with CO_2 bubble generation at the acidic tumoral environment. The DOX-$CaCO_3$-MNPs displayed effective antitumor therapeutic activity in tumor-bearing mice. The concept described in this work may serve as a useful guide for development of various theranostic nanoparticles for US imaging and therapy of various cancers.

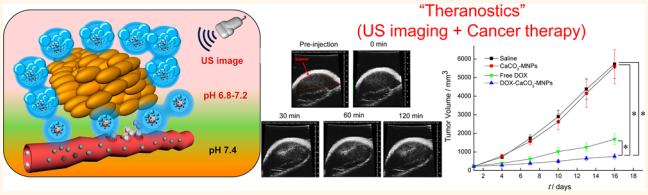

KEYWORDS: theranostics · carbon dioxide · mineralization · nanobubble · ultrasound · drug delivery

Ultrasound (US) is a noninvasive real-time imaging modality that has many advantages, such as safety, low cost, and easy access to the public.[1−3] Currently, gas-filled echogenic microbubbles are used as a US contrast agent to improve the US image quality.[4−9] They are primarily used for imaging of various organs and blood vessels but are not equipped with functionalities for imaging at tumor tissues. Recently, microbubbles with surface-conjugated ligands for specific molecular markers were developed as targeted contrast agents for tracking biological processes of tumor angiogenesis.[10,11] This targeted US imaging, based on the microbubbles, may play a significant role that can broaden the application boundary of a US imaging to tumor diagnosis. However, due to their large size (*ca.* 1−8 μm), the microbubbles are predominantly located in vascular systems after i.v. administration and do not permeate into host tumoral environments by tissue extravasation.[1,12] For this reason, the application of current micron-size bubbles is limited to the imaging of intravascular processes.[10−14] Moreover, the gas-filled microbubbles suffer from inherent drawbacks, such as low stability and short half-life in blood due to rapid diffusion of gas species through defects of the microbubbles.[15,16]

Recently, we proposed a "gas-generating" polymeric nanoparticle system that could

* Address correspondence to schlee@khu.ac.kr, ikwon@kist.re.kr.

Received for review March 14, 2014 and accepted January 5, 2015.

Published online January 05, 2015
10.1021/nn506210a

generate carbon dioxide (CO_2) bubbles by hydrolysis of carbonate side chains and showed its potential as a US contrast agent.[17] This gas-generating solid nanoparticle may overcome the limitations of current gas-filled microbubbles because gas-generating nanoparticles may circulate stably in the bloodstream and can effectively accumulate in tumor tissues by the enhanced permeation and retention effect. In addition, the gas-generating nanoparticles continuously generate CO_2 nanobubbles that coalesce into microbubbles, allowing for the persistence of strong echogenic US imaging. Although polycarbonate-based gas-generating nanoparticles expressed several advantages, they have a weakness in effective tumor imaging in that they did not have gas-generating properties in response to tumoral environments.

In recent years, theranostic nanoparticles, which integrate imaging and therapeutic functionalities, have played a central role in the improvement of tumor treatment.[18−23] Diverse theranostic nanoparticles for tumor imaging have been a major research target for various imaging tools, such as positron emission tomography, magnetic resonance, computed tomography, and optical imaging.[24−27] However, the development of a theranostic nanoparticle that expresses US imaging and therapeutic functions for tumor treatment is an unexplored field. Therefore, it is challenging to develop theranostic nanoparticles that not only generate gas bubbles for tumoral US imaging but also simultaneously provide therapeutic activity for tumor treatment.

Herein, we aim to develop a gas-generating calcium carbonate ($CaCO_3$) mineralized nanoparticle ($CaCO_3$-MNP) that can generate CO_2 bubbles and trigger the release of anticancer drugs at tumoral acidic pH for US imaging and simultaneous therapy of tumors. The extracellular pH of tumor tissues (6.8−7.2) is lower than that of normal tissues (pH 7.4) because of up-regulated glycolysis, which produces lactates and protons in an extracellular environment.[28,29] We chose the lower pH of tumor tissues as a target for tumoral US imaging and therapeutic strategies.

RESULTS AND DISCUSSION

Block Copolymer Mediated Mineralization for Doxorubicin-Loaded $CaCO_3$ Nanoparticles. Our recent research has been focused on biomimetic mineralization of various templates, such as assembly of nanoparticles and mesoporous nanoparticles, to generate pH-controlled drug-releasing nanocarriers for efficient tumor therapy.[30−32] In this work, our key strategy is to prepare doxorubicin (DOX)-loaded mineralized nanoparticles (DOX-$CaCO_3$-MNPs) by block copolymer templated $CaCO_3$ mineralization in the presence of calcium cations (Ca^{2+}), carbonate anions (CO_3^{2-}), and positively charged DOX. Figure 1 shows the overall process for fabrication of the DOX-$CaCO_3$-MNPs and how the mineralized nanoparticle enables US imaging at tumoral environments (pH 6.8−7.2) and facilitates DOX release at tumor tissues. As shown in Figure 1b, the inorganic mineral $CaCO_3$ is known to react with protons and dissolve to generate CO_2 gas in an acid environment.[33] For preparation of mineralized nanoparticles, the block copolymer (poly(ethylene glycol)-*b*-poly(L-aspartic acid) (PEG-PAsp)) was added during $CaCO_3$ mineralization (Figure 1a). The anionic PAsp block of PEG-PAsp can act as a mineral-nucleating and growth template by participating in the formation of the $CaCO_3$ core. The PEG block forms a hydrated shell and may contribute to colloidal stability in the aqueous phase. In brief, an aqueous Ca^{2+} solution was added to a stirred solution of PEG-PAsp to enable electrostatic interaction of Ca^{2+} with anionic aspartate moieties of PEG-PAsp, and DOX, which is positively charged, was subsequently added to the solution mixture. In the second step, an aqueous solution of CO_3^{2-} was added dropwise to the solution mixture to induce formation of double ionic layers around the PAsp moieties. This induced ionic supersaturation triggered the growth of $CaCO_3$ minerals. The prolonged mineralization induced coalescence of mineralized species for the DOX-$CaCO_3$-MNPs. During PEG-PAsp templated mineralization, DOX could be readily loaded *in situ* within the $CaCO_3$ core through ionic interaction. To remove residual ionic species and DOX, the solution mixture was dialyzed against excess water (pH 8.0). To prevent uncontrolled rapid growth of $CaCO_3$ in the aqueous phase and selectively induce mineral growth around the acidic PAsp blocks, the stoichiometric molar ratio of [Asp]/[Ca^{2+}]/[CO_3^{2-}] was fixed at 1:1:1. It was found that a higher or lower feed molar ratio of [Asp] to [Ca^{2+}]/[CO_3^{2-}], such as 1:2:2 or 1:0.5:0.5, resulted in either the formation of large, irregular aggregates or the ineffective formation of mineralized particles (Figure S1a in the Supporting Information).

Using the optimal stoichiometric feed ratio ([Asp]/[Ca^{2+}]/[CO_3^{2-}] = 1:1:1), we obtained uniform and spherical DOX-loaded nanoparticles, as analyzed by transmission electron microscopy (TEM) (Figure 2a). The particle size and morphology of the DOX-$CaCO_3$-MNPs were dependent on mineralization time (Figure S1b and Table S1 in the Supporting Information).

As mineralization time increased from 0.5 to 12 h, the mean hydrodynamic diameter of the DOX-$CaCO_3$-MNPs increased from 145.2 ± 55.6 to 240.8 ± 8.1 nm. In addition, morphology of the DOX-$CaCO_3$-MNPs was also affected by mineralization time. At 0.5 h, the DOX-$CaCO_3$-MNPs adopted an irregular shape, most likely due to immature mineral growth and coalescence. The TEM image showed broad distribution of particle sizes, ranging from approximately 10 to 200 nm. In contrast, after increasing mineralization time (from 1 to 12 h), the morphology of the

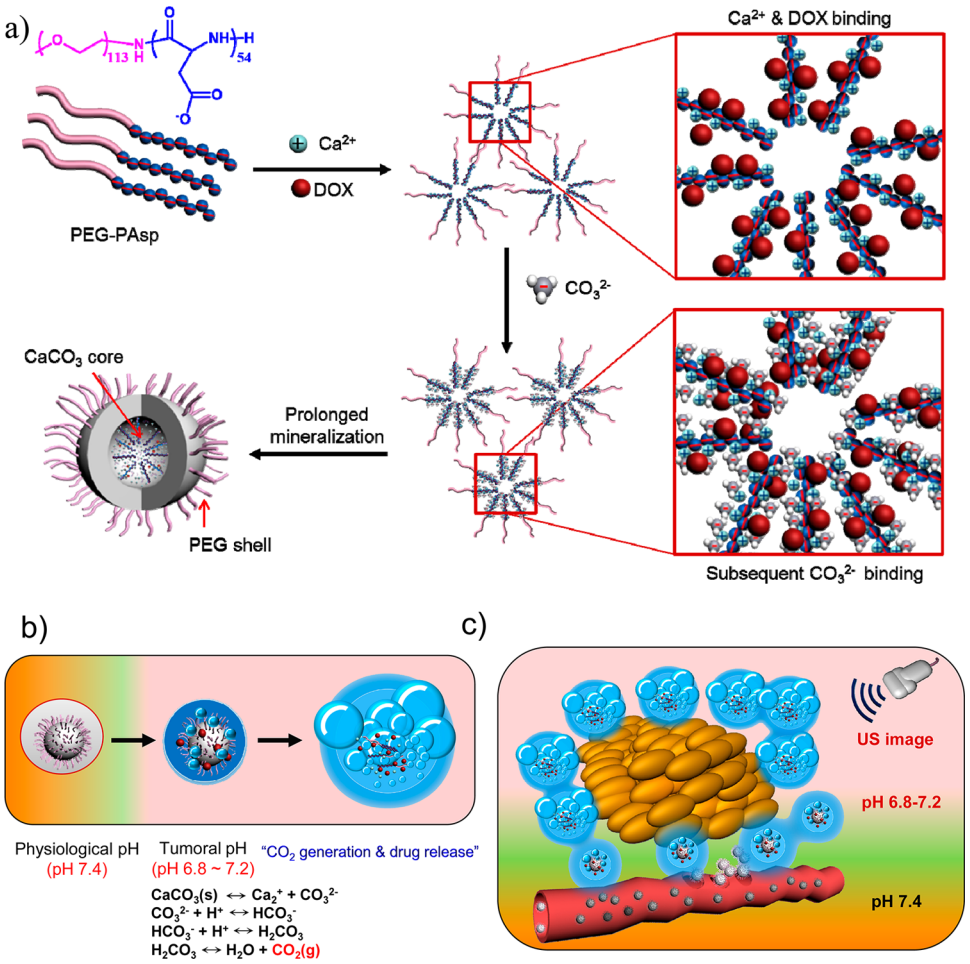

Figure 1. Schematic illustration of (a) fabrication process of DOX-$CaCO_3$-MNPs, (b) mechanism of CO_2 generation and drug release, and (c) bubble generation and drug release after accumulation of DOX-$CaCO_3$-MNPs at tumor tissues.

DOX-$CaCO_3$-MNPs was found to be a regular spherical shape, which was reflected in narrower polydispersities (Table S1 in the Supporting Information). Using dynamic light scattering, the stability of the DOX-$CaCO_3$-MNPs in a serum solution (50% fetal bovine serum (FBS) in a phosphate buffered saline (PBS) solution) was estimated. The DOX-$CaCO_3$-MNPs exhibited excellent colloidal stability in serum solutions, as judged by the constant mean diameter and scattered light intensities (SLI) for up to 24 h (Figure 2b).

To estimate the effect of PEG-PAsp on formation of the stable DOX-$CaCO_3$-MNPs, the mineralization was performed in the presence or absence of PEG-PAsp. After $CaCO_3$ mineralization, the solution was centrifuged at 1500 rpm for 5 min. During the mineralization process, the solution without PEG-PAsp produced a large amount of precipitates in the bottom because of uncontrolled nucleation and mineral growth in the aqueous phase (Figure S2 in the Supporting Information). On the other hand, the mineralized solution prepared in the presence of PEG-PAsp maintained a homogeneous dispersion even after centrifugation. These results suggest that PEG-PAsp plays a critical role in the mineralization process and formation of the nanosized DOX-$CaCO_3$-MNPs with colloidal stability.

TEM-associated energy-dispersive X-ray spectroscopy (EDX) analysis showed that the DOX-$CaCO_3$-MNPs predominantly contained Ca, C, and O, which belong to $CaCO_3$ (Figure 2c). Fourier transform infrared (FT-IR) analysis showed that DOX-loaded mineralized nanoparticles showed stretching bands at 877 and 746 cm^{-1}, indicating successful formation of $CaCO_3$ minerals in a vaterite form (Figure 2d).[34] The X-ray powder diffraction (XRD) pattern also showed that DOX-$CaCO_3$-MNPs exhibited characteristic peaks of hexagonal vaterite polymorphs (Figure S3 in the Supporting Information).

pH-Dependent CO_2 Generation from DOX-$CaCO_3$-MNPs. The quantitative analysis of CO_2 gas generation was examined using a mass spectrometer. The amount of CO_2 was estimated by monitoring the peak at 44 Da.[17] As controls, the amount of residual CO_2 present in a buffer solution (pH 7.4) and a PEG-PAsp-containing buffer solution (pH 7.4) was measured. As shown in Figure 3a, the amount of CO_2 from the PEG-PAsp solution (0.018 cc/atm) was almost the same as the amount of residual CO_2 in the buffer solution, reasonably indicating that

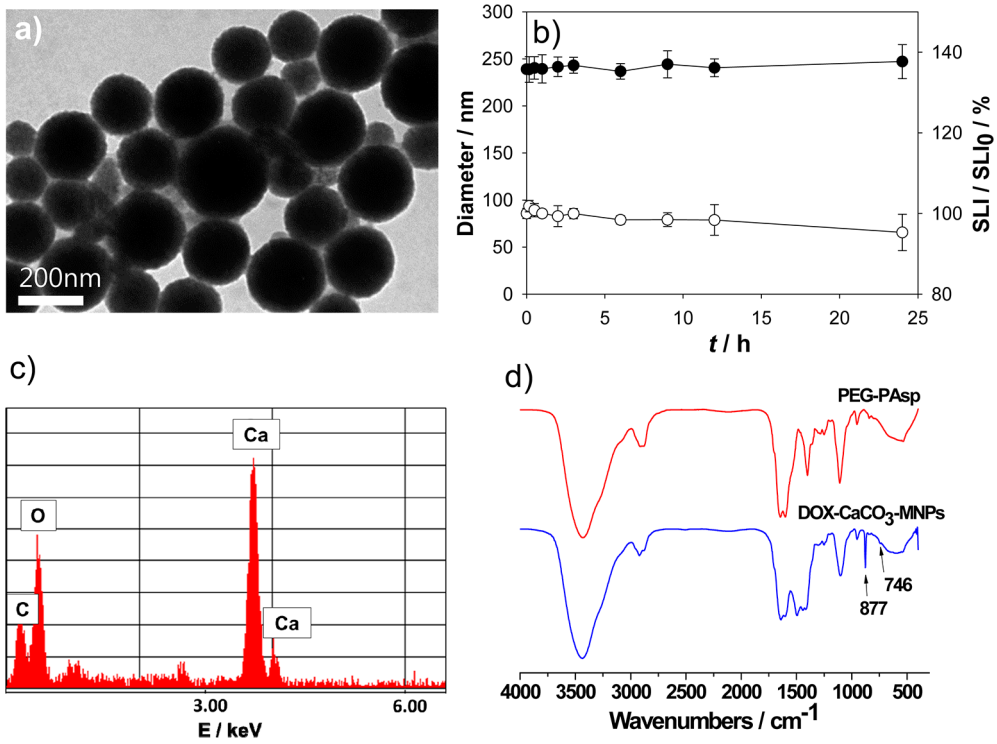

Figure 2. (a) TEM image of DOX-$CaCO_3$-MNPs after mineralization for 12 h. (b) Time-dependent changes of the mean diameter (●) and the ratio of scattered light intensities (○) of DOX-$CaCO_3$-MNPs in the serum-containing PBS solution at 37 °C (n = 3). (c) TEM-associated EDX spectra. (d) FT-IR spectra of PEG-PAsp and DOX-$CaCO_3$-MNPs. SLI refers to scattering light intensity.

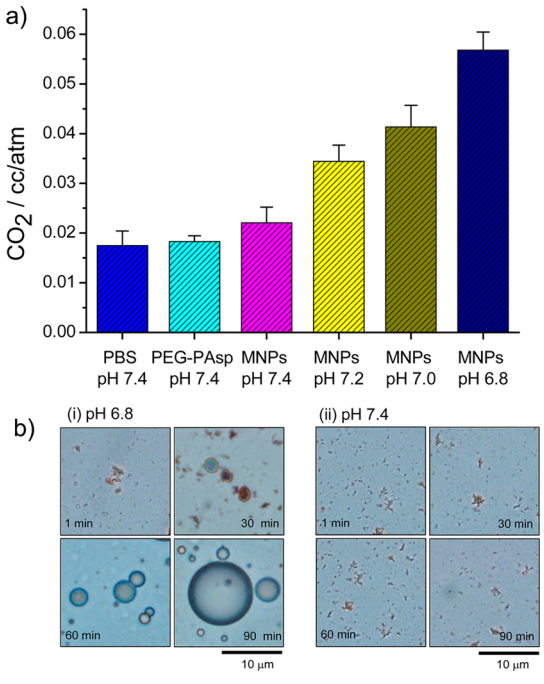

Figure 3. (a) Amount of CO_2 generated from DOX-$CaCO_3$-MNPs at various pH and (b) optical micrographs of CO_2-generating profiles of sub-micron-size aggregates of DOX-$CaCO_3$-MNPs incubated in PBS ((i) pH 6.8 and (ii) pH 7.4) for 90 min.

PEG-PAsp had no effect on CO_2 generation. To analyze the dependency of pH on CO_2 generation, the amount of generated CO_2 from the DOX-$CaCO_3$-MNPs was measured under pH controls (from pH 7.4 to 6.8). Although CO_2 was generated from the DOX-$CaCO_3$-MNPs at pH 7.4, the level was as low as 0.022 cc/atm, a negligible amount similar to control groups. In contrast, as the pH level decreased, the amount of CO_2 generated from the DOX-$CaCO_3$-MNPs dramatically increased to 0.034, 0.041, and 0.057 cc/atm for pH 7.2, 7.0, and 6.8, respectively. Compared to the amount of CO_2 generated at pH 7.4, these CO_2 amounts corresponded to an increase of 54.5, 86.4, and 159.0%, respectively. The increase in CO_2 generation at lower pH level may be due to faster dissolution of the $CaCO_3$ mineral phase. This pH-dependent CO_2 generation from $CaCO_3$ phases can be explained by the inherent solution behavior of $CaCO_3$. According to the chemical equilibrium of $CaCO_3$ in the aqueous phase (Figure 1b), three major carbonate species (CO_3^{2-}, HCO_3^-, and H_2CO_3) exist, and their distribution varies depending on solution pH. It is worth noting that the level of H_2CO_3 (carbonic acid), the major source for CO_2 generation, becomes dramatically dominant below pH 7.0, while it exists at an insignificant level at pH 7.4. This distinguished gas-generating feature of the DOX-$CaCO_3$-MNPs at weakly acidic tumoral pH supports our assumption that $CaCO_3$ mineralized nanoparticles may sense the acidic pH of tumors, causing CO_2 bubble generation.

We visualized the generation of CO_2 bubbles from the DOX-$CaCO_3$-MNPs using optical microscopy. Because the individual DOX-$CaCO_3$-MNPs are nanosized

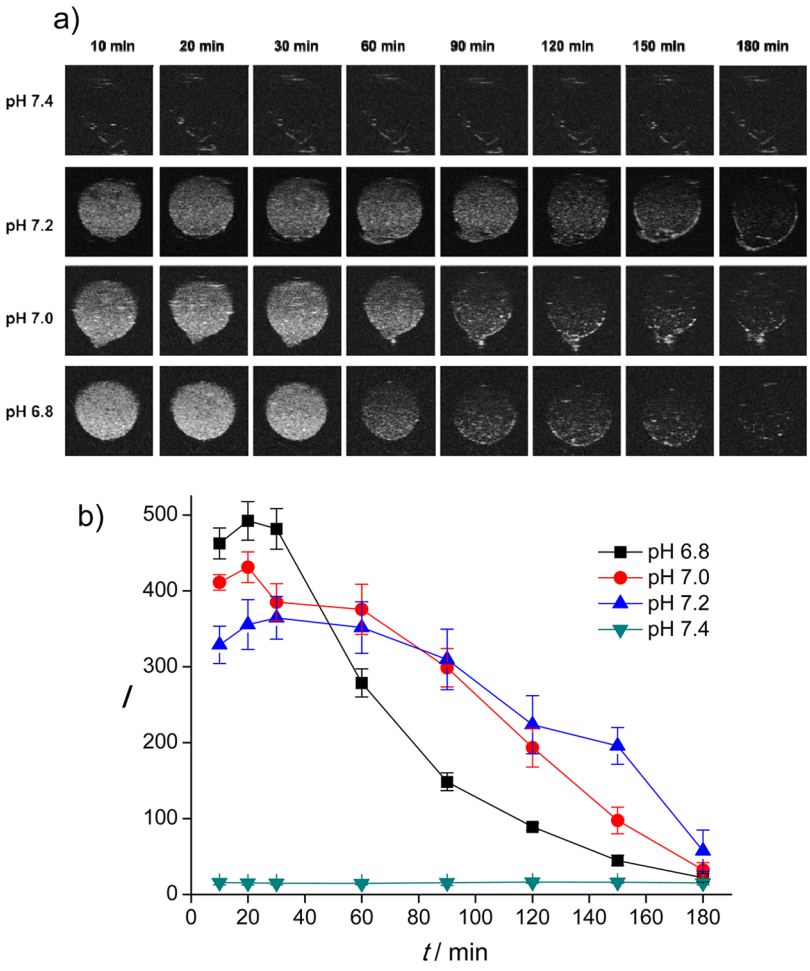

Figure 4. (a) *In vitro* US images and (b) time-dependent US contrast intensity from DOX-$CaCO_3$-MNPs at various pH. *I* refers to the intensity in arbitrary units, and *t* refers to time.

and cannot be identified using optical microscopy, we used a sub-micron-size aggregate of the DOX-$CaCO_3$-MNPs of approximately 1 μm to visualize the direct bubble formation at tumoral pH. It is interesting to note that, at 30 min postincubation at pH 6.8, the sub-micron-size aggregate expanded to form larger bubbles of approximately 3 μm (Figure 3b). As the incubation time increased to 90 min, the bubble diameter increased to approximately 10 μm, possibly due to the expansion or coalescence of nanobubbles into microbubbles. These micron-size bubbles may serve as echogenic contrast agents by displaying enhanced reflection at tumor tissues. As expected from a quantification assay in Figure 3a, we could not observe any substantial microbubble formation from DOX-$CaCO_3$-MNPs at pH 7.4 (Figure 3b).

pH-Dependent *In Vitro* Echogenic Properties of DOX-$CaCO_3$-MNPs. Next, we monitored the *in vitro* echogenic performance of the DOX-$CaCO_3$-MNPs as a function of pH using an agar gel phantom test at 37 °C. As shown in Figure 4a, the DOX-$CaCO_3$-MNPs at pH 7.4 showed no significant contrast signals under a US field, most likely because the DOX-$CaCO_3$-MNPs did not generate CO_2 bubbles sufficient for echogenic reflection. This observation is consistent with the results of the pH-dependent quantification assay of CO_2 generation (Figure 3a). In contrast, US contrast images from the DOX-$CaCO_3$-MNPs were significantly enhanced at weakly acidic pH conditions (pH 7.2, 7.0, and 6.8). At pH 7.2, the echo intensity persisted for more than 150 min, and the half-life of echo signals is up to 106 min (Figure 4b). Notably, as the pH level decreased from 7.2 to 7.0 and 6.8, the echo intensity of the DOX-$CaCO_3$-MNPs was initially enhanced, while the half-life of US signals decreased to 83.0 and 48.1 min, respectively. This is a well understood phenomenon in which the higher echo intensity at lower pH levels is ascribed to facilitated formation of larger amounts of CO_2 bubbles due to faster dissolution of $CaCO_3$ phases, and the echo signals faded away earlier than at higher pH. The excellent echo persistence at weak acidic pH can be attributed to the retarded ionization of $CaCO_3$ solid phases.[35] The contrast enhancement that arises from the DOX-$CaCO_3$-MNPs at tumoral pH indicates that generation of CO_2 bubbles was responsible for echogenic US resonation. This gas-generating feature

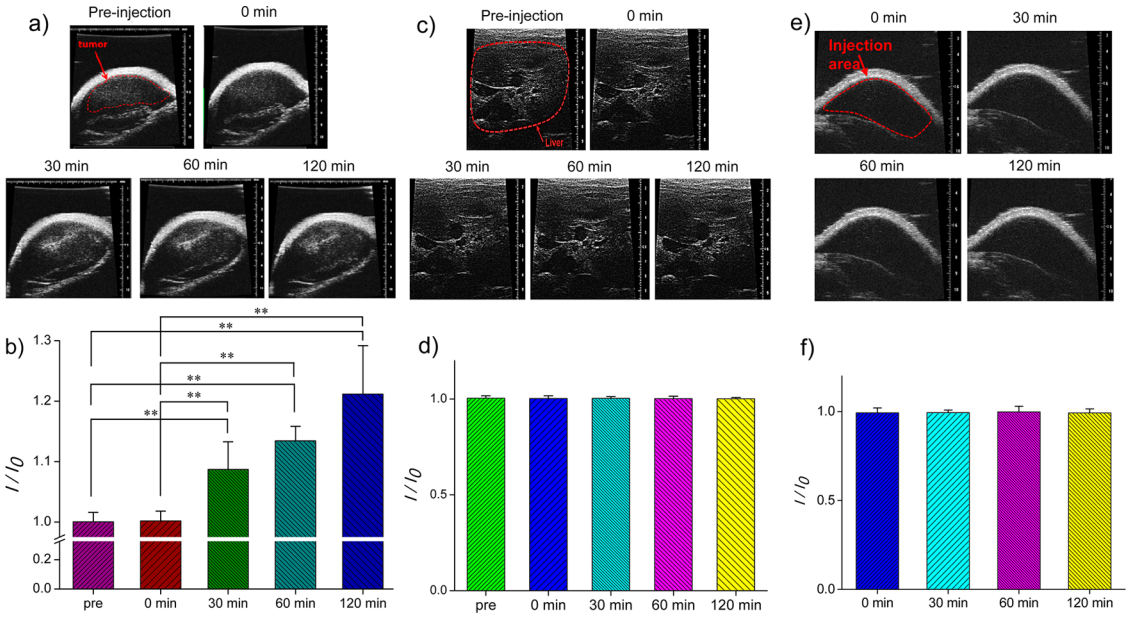

Figure 5. (a) *In vivo* US imaging of the SCC-7 tumor by intratumoral injection of DOX-$CaCO_3$-MNPs, (b) histogram of a US intensity profile of the tumor as a function of time (I_0 is the ultrasound intensity of preinjection), (c) *in vivo* US imaging of the liver by the injection of DOX-$CaCO_3$-MNPs into the liver, (d) histogram of a US intensity profile of the liver as a function of time (I_0 is the ultrasound intensity of preinjection), (e) *in vivo* US imaging of subcutaneously injected areas of DOX-$CaCO_3$-MNPs, and (f) histogram of a US intensity profile of subcutaneous areas as a function of time (I_0 is the ultrasound intensity immediately after injection). Images and data at 0 min were obtained immediately after injection. Statistical analysis: one-way ANOVA + Tukey's post hoc test ($P < 0.01$).**

at a broad range of weak acidic pH may be suitable for US imaging of tumors, which have tissue heterogeneity and diverse pH levels (pH 6.8−7.2).

***In Vivo* US Imaging of a Tumor with DOX-$CaCO_3$-MNPs.** To demonstrate potential of the DOX-$CaCO_3$-MNPs for US imaging of a tumor, we administered an intratumoral injection of a DOX-$CaCO_3$-MNP dispersion to squamous cell carcinoma (SCC-7) tumor-xenograft-bearing C3H/HeN nude mice and monitored US images as a function of time (Figure 5a,b). Immediately after injection, we could not observe any contrast enhancement at tumor tissues. Interestingly, enhancement in US images was observed within 30 min after injection. In addition, this contrast enhancement lasted up to 120 min (Figure 5b). This long echo persistence was consistently supported by *in vitro* imaging data (Figure 4a). We also observed localized spots of enhanced contrast, possibly due to adequate accumulation of mineralized nanoparticles in the tumor tissues.

In vivo results indicate that the DOX-$CaCO_3$-MNPs generated nanobubbles at tumor tissues, which coalesced into micron-size bubbles, which could generate sufficient echogenic reflectivity under a US field. To verify the imaging ability at tumor tissues, we injected a DOX-$CaCO_3$-MNP dispersion to the liver or subcutaneously to the back of tumor-free C3H/HeN mice and examined the time-dependent US imaging patterns (Figure 5c,d and Figure 5e,f). We could not observe any contrast enhancement at the liver and the subcutaneous tissues for 120 min. This suggests that the DOX-$CaCO_3$-MNPs located in the liver and subcutaneous area at physiological pH did not generate the CO_2 bubbles necessary for US contrast.

To confirm the pH-dependent generation of the echogenic signals, we measured pH of the SCC-7 tumor tissues using a pH meter and a probe for semisolid materials. pH values of the liver and the subcutaneous tissues were also measured as control experiments. Estimation of pH in human and animal tumors by insertion of pH electrodes was well-documented, and in general, the tumors were known to be more acidic than normal tissues with mean pH values of *ca.* 7.0 in tumors and 7.5 in normal tissues.[36] As shown in Figure S4 in the Supporting Information, pH of the SCC-7 tumor tissue was found to be 6.8 ± 0.1, whereas pH of the liver and the subcutaneous tissues were 7.3 ± 0.05 and 7.4 ± 0.04, respectively. The acidic pH is known as the main factor that can dissolve $CaCO_3$ to generate CO_2 molecules. Although there may exist various factors *in vivo*, these experimental supporting data based on *in vivo* pH measurements would verify that our nanoparticles generated CO_2 bubbles at an acidic pH environment of the tumor tissues. Based on this proof-of-concept study, $CaCO_3$ mineralized nanoparticles can provide the opportunity for visualization of the low pH environment in tumors by a noninvasive and real-time US imaging system.

pH-Controlled DOX Release and $CaCO_3$ Dissolution Behavior. The block copolymer templated $CaCO_3$ mineralization in this work is beneficial as it is a simple process that can produce nanocarriers capable of loading diverse ionic cancer therapeutics *in situ* within the $CaCO_3$ core.

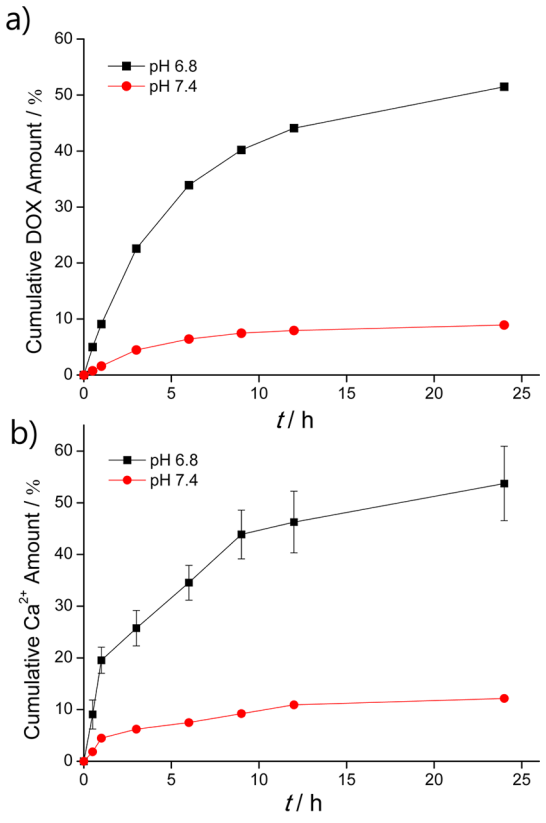

Figure 6. (a) DOX release profiles from DOX-$CaCO_3$-MNPs at different pH values of 6.8 and 7.4 (n = 3) and (b) kinetics of calcium dissolution from DOX-$CaCO_3$-MNPs under pH control (n = 3).

In our system, the $CaCO_3$ mineral serves not only as a CO_2 bubble-generating precursor for US imaging but also as a cargo that can stably load anticancer drugs and release these drugs under pH control. To verify the drug-releasing ability of the DOX-$CaCO_3$-MNPs at tumoral pH, we examined the profiles of DOX release in aqueous buffer solutions of pH 7.4 and 6.8 (Figure 6a). The loading content of DOX in the DOX-$CaCO_3$-MNPs was 7.1 wt %. It is well-documented that, when the pH level decreases, aqueous solubility of $CaCO_3$ exponentially increases. $CaCO_3$ is known to react with acids to produce carbonic acid, which decreases the concentration of CO_3^{2-}, thereby making $CaCO_3$ more soluble.[35] The release of DOX from the DOX-$CaCO_3$-MNPs was significantly inhibited at pH 7.4. This indicates that the DOX-$CaCO_3$-MNPs can maintain the solid nanoparticle structure at physiological pH due to low solubility of $CaCO_3$. In contrast, at pH 6.8, the DOX-$CaCO_3$-MNPs exhibited rapid DOX release rate, with 44% of DOX released within 12 h, indicating the facilitated dissolution of DOX-loaded $CaCO_3$ phases. To further analyze this pH-dependent release behavior, the kinetics of Ca^{2+} dissolution from the DOX-$CaCO_3$-MNPs was also investigated (Figure 6b).

At pH 7.4, the DOX-$CaCO_3$-MNPs showed a retarded release of Ca^{2+} ions of less than 12%. In contrast, at pH 6.8, we found accelerated dissolution of $CaCO_3$ mineral phases. The rapid dissolution of $CaCO_3$ minerals at the lower pH is a reasonable finding, as the aqueous solubility of $CaCO_3$ increases proportionally to the concentration of proton ions.[35] It is of great interest to note that this pH-dependent kinetics of $CaCO_3$ dissolution corresponds directly to the DOX release. This result suggests that the DOX-$CaCO_3$-MNPs may stably hold DOX in blood and trigger DOX release at the target tumor tissue.

***In Vitro* Cytotoxicity of DOX-$CaCO_3$-MNPs.** The cytotoxicity of the DOX-$CaCO_3$-MNPs was evaluated on SCC-7 cells using a cell counting kit-8 assay. Importantly, the DOX-free $CaCO_3$-MNPs did not show any noticeable cytotoxicity on the SCC-7 cells for concentrations up to 500 μg/mL (Figure S5 in the Supporting Information). *In vitro* cytotoxicity of free DOX and the DOX-$CaCO_3$-MNPs was also estimated. Free DOX significantly decreased the viability of SCC-7 cancer cells in a dose-dependent manner (Figure S6 in the Supporting Information). Although the DOX-$CaCO_3$-MNPs also exhibited a cytotoxic effect, SCC-7 cells treated with the DOX-$CaCO_3$-MNPs retained higher viabilities than cells exposed to free DOX (Table S2 in the Supporting Information). The somewhat lower toxicity of the DOX-$CaCO_3$-MNPs, compared to free DOX, was most likely due to the gradual release of DOX within acidic compartments of the cell (endo/lysosomes) because the DOX release, under our *in vitro* experimental condition, was triggered by $CaCO_3$ dissolution within cellular acidic environment.

Cellular Uptake and Intracellular Distribution of DOX-$CaCO_3$-MNPs. To monitor cellular uptake of DOX-$CaCO_3$-MNPs, we prepared fluorescein isothiocyanate (FITC)-incorporated DOX-$CaCO_3$-MNPs. The intracellular distribution of FITC-incorporated DOX-$CaCO_3$-MNPs was monitored by confocal laser scanning microscopy (CLSM). After 1 h incubation, the SCC-7 cells treated with FITC-incorporated DOX-$CaCO_3$-MNPs displayed a green and red fluorescence at the cytosol and a negligible red fluorescence within the nuclei (Figure S7 in the Supporting Information). This indicates the uptake of the nanoparticles and their location at the acidic endo/lysosomal compartments. After a further incubation of 5 h, a stronger DOX fluorescence was found in nuclei than in cytosols, possibly due to the DOX release triggered by dissolution of DOX-loaded $CaCO_3$ cores in the acidic compartments. On the other hand, the majority of green FITC fluorescence was still found in the cytosol, not in the nuclei. This indicates that the residual FITC-incorporated nanoparticles or FITC-labeled PEG-PAsp, generated by the nanoparticle dissolution in endo/lysosomes, stayed at the cytosols.

As an additional experiment to verify the cellular uptake of the $CaCO_3$-MNPs, the dissolution of the $CaCO_3$ cores within acidic cellular environments was visualized using an acetoxymethyl ester derivative of Rhod-2 (Rhod-2/AM), a membrane-permeable

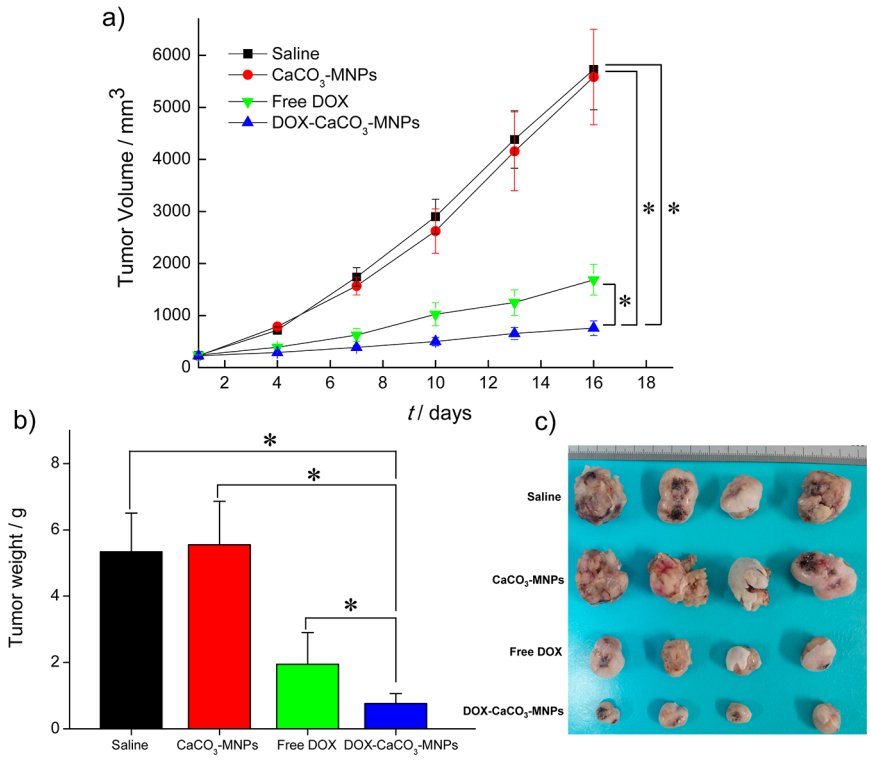

Figure 7. (a) Changes in tumor volumes after injection of saline, $CaCO_3$-MNPs, free DOX, and DOX-$CaCO_3$-MNPs; (b) tumor weights after 16 days post-treatment; and (c) images of excised tumors of each group with controls (saline and $CaCO_3$-MNPs), free DOX, and DOX-$CaCO_3$-MNPs after 16 days post-treatment ($n = 4$). The results represent the means ± SD ($n = 4$). Statistical analysis: one-way ANOVA + Tukey's post hoc test (*$P < 0.05$).

derivative of a calcium-specific dye Rhod-2. Upon cellular internalization, Rhod-2/AM is rapidly hydrolyzed to Rhod-2 by endogenous esterases, and Rhod-2 binds with free Ca^{2+} to form the Rhod-2-Ca^{2+} complex, which generates the red fluorescence.[37,38] As shown in Figure S8 in the Supporting Information, the cells of the Rhod-2/AM-treated positive control displayed a weak red fluorescence due to the native Ca^{2+} in the cytosol. It is noted that the cells treated with $CaCO_3$-MNPs exhibited a stronger red fluorescence, compared with the positive control and PEG-PAsp-treated cells. In addition, as the concentration of $CaCO_3$-MNPs increased from 100 to 300 μg/mL, the stronger fluorescence of the Rhod-2-Ca^{2+} complex was observed. This result strongly supports that the $CaCO_3$-MNPs were internalized within cells and localized within acidic endo/lysosomes to dissolve $CaCO_3$ cores, thereby generating Ca^{2+} ions.

The cellular uptake of DOX-$CaCO_3$-MNPs was monitored by CLSM. The acidic cellular compartment was labeled with green fluorescent LysoTracker as an indicator. As shown in Figure S9a in the Supporting Information, after 1 h incubation of SCC-7 cells with free DOX, almost all the DOX molecules were located in the nucleus, indicating fast accumulation by diffusion across the cellular membrane. In contrast, SCC-7 cells treated with DOX-$CaCO_3$-MNPs, after 1 h incubation, exhibited a bright red DOX fluorescence within the acidic compartments and a negligible red fluorescence within the nuclei (Figure S9b in the Supporting Information). After 6 h of incubation, a strong fluorescence was found in the nuclei, which can be ascribed to the released DOX from internalized DOX-$CaCO_3$-MNPs (Figure S9c in the Supporting Information). This indicates that a triggering factor for DOX release was the dissolution of DOX-loaded $CaCO_3$ minerals in acidic cellular compartments. Therefore, it might be suggested that the $CaCO_3$ core can effectively hold DOX before cellular uptake, and the DOX release can be facilitated within endo/lysosomes by the dissolution of the $CaCO_3$ core. From the *in vitro* experiments, we confirmed that the DOX-$CaCO_3$-MNPs have the ability to inhibit proliferation of SCC-7 cells by delivering DOX within the cells.

***In Vivo* Antitumor Efficacy of DOX-$CaCO_3$-MNPs.** The anticancer therapeutic efficacy of the DOX-$CaCO_3$-MNPs was examined in SCC-7 tumor-bearing mice. Free DOX (10 mg/kg) and the DOX-$CaCO_3$-MNPs (10 mg/kg of DOX) were administered with single intratumoral injection. Figure 7a shows the changes in tumor volumes in nude male mice after injection of saline, the $CaCO_3$-MNPs, free DOX, the DOX-$CaCO_3$-MNPs. The DOX-free control groups (saline and $CaCO_3$-MNPs) did not show any noticeable inhibition of tumor growth. In contrast, the DOX-$CaCO_3$-MNPs are significantly more efficacious in tumor reduction than control groups and

the free DOX. At 16 days postinjection, free DOX suppressed the tumor weight by 61% and the DOX-$CaCO_3$-MNPs decreased the tumor weight by 85%, compared to the saline-treated mice (Figure 7b,c). In our experimental design, the anticancer efficacy was evaluated for a few weeks because this time period is enough to confirm whether our newly developed theranostic nanoparticles exhibit the improved efficacy for cancer therapy, compared to the free anticancer drug.

This enhanced antitumor therapeutic efficacy of the DOX-$CaCO_3$-MNPs might be explained by the delayed clearance of the DOX-$CaCO_3$-MNPs at the tumor site due to the enhanced retention properties of the nanoparticles.[32] To estimate time-dependent DOX distribution after intratumoral injection, we obtained noninvasive real-time fluorescence imaging of DOX. The tumor tissues, treated with free DOX, generated strong red fluorescence for 12 h initially, and thereafter, the fluorescence intensity rapidly decreased to 23.8% of the initial intensity (Figure S10a,b in the Supporting Information). In contrast, for DOX-$CaCO_3$-MNP-treated tumors, the strong fluorescence of DOX was maintained for up to 8 days and 74.1% of the initial intensity was maintained. At 8 days postinjection, the tumor tissues were isolated for observation of *ex vivo* images. It was found that the total fluorescence photon counts in the DOX-$CaCO_3$-MNP-treated tumors were significantly much higher than the tumors treated with free DOX (Figure S10c,d in the Supporting Information). This real-time imaging experiment for DOX distribution strongly supported the prolonged retention of DOX-$CaCO_3$-MNPs at tumor tissues and the continuous release of DOX from the DOX-$CaCO_3$-MNPs.

This is consistent with long-lasting echo signals of the DOX-$CaCO_3$-MNPs at tumor tissues, which were evaluated using *in vivo* US imaging of tumors (Figure 5a). Furthermore, DOX was released simultaneously with CO_2 bubble generation at the acidic tumoral environment and could be rapidly taken up by tumor cells, allowing for the enhanced antitumor effect.

CONCLUSIONS

In summary, we successfully constructed DOX-loaded $CaCO_3$ (vaterite) mineralized nanoparticles through a block copolymer templated *in situ* mineralization approach. The nanoparticles with well-defined morphology and size were obtained by controlling the feed ratio of ions (Ca^{2+} and CO_3^{2-}) to anionic Asp units and mineralization time. The nanoparticles generated CO_2 bubbles at tumoral pH and simultaneously triggered the release of DOX. The DOX-$CaCO_3$-MNPs have great potential as a theranostic agent for simultaneous US imaging and therapy of cancers. The approach suggested in this work may provide a valuable direction for useful theranostic nanoparticles with improved US imaging and anticancer therapeutic functions.

MATERIALS AND METHODS

Materials. α-Methoxy-ω-aminopoly(ethylene glycol) (CH_3O-PEG-NH_2), M_n = 5000 g/mol, was purchased from IDBIOCHEM Inc. (Seoul, Korea). β-Benzyl L-aspartate (BAsp) and doxorubicin hydrochloride (DOX·HCl) were purchased from Sigma Co. (St. Louis, MO) and used without further purification. Triphosgene was purchased from Aldrich Co. (Milwaukee, WI) and used as received. *N*,*N*-Dimethylformamide (DMF) was dried and distilled over calcium hydride. Calcium chloride ($CaCl_2$) and sodium carbonate (Na_2CO_3) were of the reagent grade. β-Benzyl L-aspartate *N*-carboxyanhydride (BAsp-NCA) of high purity was synthesized by the Fuchs-Farthing method using triphosgene.[39] All other chemicals were of analytical grade and used without further purification.

Synthesis of PEG-*b*-PAsp Copolymer (PEG-PAsp). A poly(ethylene glycol)-*b*-poly(L-aspartic acid) copolymer (PEG-PAsp) that has EG units of 113 and Asp units of 54 was synthesized by a modified procedure established in our laboratory.[40] In brief, to a stirred solution of CH_3O-PEG-NH_2 (1.5 g, 0.3 mmol) in dry DMF (10 mL) was added BAsp-NCA (4.5 g, 18 mmol) at 35 °C under nitrogen. After 24 h, PEG-PBAsp was isolated by repeated precipitation from DMF into diethyl ether. Yield: 83%. Finally, hydrolytic deprotection of benzyl groups in PEG-PBAsp was performed by treating the block copolymer (2 g) with 0.1 N NaOH (200 mL). The aqueous solution was then dialyzed using a membrane (molecular weight cutoff (MWCO): 1000) for 24 h, followed by freeze-drying. The polydispersity index (M_w/M_n), estimated by gel permeation chromatography, was 1.06.

Preparation of DOX-Loaded $CaCO_3$ Mineralized Nanoparticles (DOX-$CaCO_3$-MNPs). DOX-$CaCO_3$-MNPs were prepared by a PEG-PAsp templated *in situ* mineralization technique. PEG-PAsp (100 mg) was dissolved in 4 mL of distilled water (pH 8.0) for 1 h, and then an aqueous $CaCl_2$ solution (53.2 mg, 0.48 mmol) of 2 mL was first added to a stirred solution and equilibrated for 2 h under stirring at 800 rpm. The DOX solution (10 mg, 2 mL) was subsequently added and stirred in the dark at room temperature for 2 h, and an aqueous solution (2 mL) of Na_2CO_3 (50.8 mg, 0.48 mmol) was then slowly dropped into the reaction mixture. For a stoichiometric ratio, the molar concentration ratio of [Asp]/[Ca^{2+}]/[CO_3^{2-}] was 1:1:1. The mixed solution was stirred magnetically at 800 rpm at room temperature for 12 h. The solution was centrifuged and dialyzed to remove unreacted ionic species, and the dialysate was lyophilized to obtain the DOX-$CaCO_3$-MNPs. To determine the drug loading content and loading efficiency, DOX-$CaCO_3$-MNPs were stirred in 1 N HCl solution for 30 min. The fluorescence emission intensity was measured at 588 nm (excitation at 480 nm). The drug loading content was calculated based on the standard curve obtained using DOX.

Characterization of DOX-$CaCO_3$-MNPs. Dynamic light scattering measurements were performed using a 90 plus particle size analyzer (Brookhaven Instruments Corporation). The scattered light of a vertically polarized He−Ne laser (632.8 nm) was measured at an angle of 90° and was collected on an autocorrelator. The hydrodynamic diameters (*d*) of micelles were calculated by using the Stokes−Einstein equation.[41] The polydispersity factor of DOX-$CaCO_3$-MNPs, represented as μ_2/Γ^2, where μ_2 is the second cumulant of the decay function and Γ is the average characteristic line width, was calculated from the cumulant method.[41] The morphology of DOX-$CaCO_3$-MNPs was examined by transmission electron microscopy (JEM-2000EX, JEOL Tokyo, Japan). DOX-$CaCO_3$-MNPs were analyzed by TEM-associated EDX to reveal atomic components. EDX measurement was carried out using JEOL JEM-2100F equipped with

an EDAX Genesis series TEM at 200 kV. XRD measurements were performed with a Rigaku D/max-RB apparatus (Tokyo, Japan) powder diffractometer and image-plate photography using graphite-monochromatized Cu Kα radiation (λ = 1.542 Å). Data were collected from 10 to 60° with a step size of 0.05 and step time of 5 s. FT-IR spectra of samples were measured with PerkinElmer FT-IR system (Spectrum GX) at room temperature under a stream of nitrogen gas. The mixed powder of samples and KBr was pressed for pellets of the IR window and then dried in a vacuum oven for 24 h. FT-IR spectra of polymer sample were measured at a resolution of 4 cm^{-1}.

Stability of DOX-$CaCO_3$-MNPs. The physical stability of the DOX-$CaCO_3$-MNPs was evaluated in serum-containing solutions. The effect of serums on the physical stability of DOX-$CaCO_3$-MNPs in aqueous media was estimated by dynamic light scattering analysis. For the stability in serum conditions, the stability of DOX-$CaCO_3$-MNPs (1 mg/mL) in the serum-containing PBS solution (50% FBS, pH 7.4) was examined. The mean diameter of the nanoparticles was monitored, and scattered light intensity (SLI) was compared to the initial scattered light intensity (SLI_0).

Quantification of CO_2 Generation from DOX-$CaCO_3$-MNPs as a Function of pH. The amount of CO_2 generated from DOX-$CaCO_3$-MNPs was measured with a quadrupole mass spectrometer (Prisma QME 200, Germany) equipped with a Faraday cup detector. The vapor was analyzed with an emission current of 0.058 mA, an electron energy of 8 eV, and resolution of 750. A sample chamber was vacuumed with a turbo molecular pump (Pfeiffer vacuum, CA, USA) and measured at room temperature. Phosphate buffer solutions at various pH (7.4, 7.2, 7.0, and 6.8, 2 mL) and 20 mg of DOX-$CaCO_3$-MNPs were placed in the sample with two branched chambers. The buffer solution in the chamber was frozen under vacuum conditions and thawed. As control experiments, the amounts of CO_2 present in the buffer solution (pH 7.4) and the PEG-PAsp-containing buffer solution (pH 7.4) were calculated. For measurement of CO_2 generated from DOX-$CaCO_3$-MNPs, DOX-$CaCO_3$-MNPs were exposed to each thawed buffer solution with variable pH. After 30 min exposure to buffer solutions, the sample was frozen and then vacuumed. The amount of generated CO_2 was calculated with an inlet volume for mass measurement.

***In Vitro* US Imaging at Various pH.** *In vitro* US imaging of DOX-$CaCO_3$-MNPs was performed in phosphate buffer solutions at various pH (7.4, 7.2, 7.0, and 6.8). An optically transparent phantom gel plate, made by embedding a 500 μL Eppendorf tube in the agarose gel (3%, w/v) and then removing the tube after the phantom gel had cooled, was used as the *in vitro* experiment. Aqueous nanoparticle solutions (25 mg/mL) were prepared at various pH. US images were obtained using VisualSonics Vevo 770 (high-resolution micro-imaging system, VisualSonics, Toronto, Canada) with the RMV 706 transducer at 40 MHz of a static state using a contrast mode. The change of US intensity for each sample was measured up to 180 min, and the US intensity of the water as a control was subtracted from the sample intensity as the normalizing process.

Visualization of CO_2 Bubbles Generated from DOX-$CaCO_3$-MNPs. A drop of nanoparticle solution (5 mg/mL) was immediately placed on slide glass after dispersion of DOX-$CaCO_3$-MNPs in phosphate buffer solutions (pH 6.8 and 7.4). The CO_2 bubble image from DOX-$CaCO_3$-MNPs was monitored for 90 min at room temperature using an optical microscope (IX71; Olympus Co. Ltd., Japan) equipped with 40× focal lens (optical magnification: 400×).

***In Vivo* US Imaging of a Xenograft Tumor.** All animal treatments and surgical procedures followed approved protocols and were performed in accordance with the Institutional Animal Care and Use Committee at Kyung Hee University. The SCC-7 xenograft tumor was grown in 7-week-old male athymic C3H/HeN nude mice (20 g, Institute of Medical Science, Tokyo) by inoculating 1.0×10^6 SCC-7 cells into the dorsal side of mice. When tumors grew to approximately 250 ± 20 mm^3 in volume, US imaging of DOX-$CaCO_3$-MNPs was investigated. Before US imaging, mice were anesthetized by inhalation of 2% isoflurane with 1% oxygen. Anesthetized mice were placed on a thermostatically controlled heating pad to maintain body temperature. Then, 100 μL of PBS solution (pH 7.4) containing DOX-$CaCO_3$-MNPs (25 mg/mL, 10 mg/kg of DOX equivalent) was administered by an intratumoral injection. The tumor was imaged with the VisualSonics Vevo 770 *in vivo* high-resolution micro-imaging system with the RMV 706 transducer at 40 MHz of a static state using a contrast mode. For normalized US signals, US intensity of the background was subtracted from the intensity from DOX-$CaCO_3$-MNPs injected in the tumor region and then divided by US intensity of the background.[42] As a control *in vivo* experiment, the DOX-$CaCO_3$-MNP dispersion was administered into the liver or subcutaneous tissues in the lower backs of anesthetized tumor-free nude mice, and then time-dependent US imaging was monitored following the identical procedure mentioned above. The statistical analysis was performed using an one-way ANOVA + Tukey's post hoc test.

Measurement of Tumor pH. SCC-7 tumor-bearing C3H/HeN nude mice (male, n = 2) were under general anesthetics with Zoletil + xylazine (30 mg/kg + 10 mg/kg, IP). Tumor sites were surgically opened using a sterile razor blade, and the tumoral pH was measured using a pH meter (Thermo Electron Corporation, Waltham, MA, USA) equipped with an electrode for semisolid types of materials (Istek, Seoul, Korea). Three random spots of each tumor were measured to compare the mean tumor pH to the mean pH of the liver and subcutaneous tissues. The pH of the liver and subcutaneous tissues was measured using an identical method used for measurement of tumor pH.

DOX Release from DOX-$CaCO_3$-MNPs. *In vitro* release profiles of DOX from DOX-$CaCO_3$-MNPs were examined in phosphate buffer solutions (pH 7.4 and 6.8). DOX-$CaCO_3$-MNPs of 1 mg/mL were dispersed in aqueous buffer solutions (1 mL) and transferred to a dialysis membrane bag (MWCO: 3500 g/mol). The release experiment was initiated by placing the dialysis bag in 10 mL of release media. The release medium was shaken at a speed of 150 rpm at 37 °C. At predetermined time intervals, samples (10 mL) were withdrawn and replaced with an equal volume of the fresh medium. The concentration of released DOX in the samples was determined by measurement of fluorescence emission intensity at 588 nm (excitation at 480 nm) based on the standard curve obtained using DOX.

Calcium Dissolution of DOX-$CaCO_3$-MNPs. *In vitro* calcium dissolution experiments of DOX-$CaCO_3$-MNPs were performed in the aqueous buffer solutions (pH 7.4 and 6.8). The DOX-$CaCO_3$-MNP solution (1 mg/mL) was sealed in a dialysis membrane bag (MWCO: 3500) and was shaken at 150 rpm at 37 °C in release media. The release medium (10 mL) was withdrawn at predetermined time intervals and replaced with an equal volume of the fresh medium. The release rate of calcium ions was monitored by taking 100 μL of the sample and diluting it in the Arsenazo III solution (2 mL, 0.2 mM) in HEPES-buffered saline (where [HEPES] = 20 mM and [NaCl] = 150 mM at pH 7.4). The absorbance of the solution at 656 nm was then measured, and the concentration of calcium ions was calculated based on the standard curve.

Cytotoxicity of DOX-$CaCO_3$-MNPs. SCC-7 cells were originally obtained from the American Type Culture Collection (Rockville, MD) and cultured in RPMI 1640 medium (Gibco BRL, Gaithersburg, MD) supplemented with 10% (v/v) heat-inactivated fetal bovine serum (Gibco BRL) and 1% (v/v) penicillin-streptomycin (Gibco BRL). Cells were cultured in a humidified incubator at 37 °C with 5% CO_2. The culture medium was replaced every 2 days. Cells were seeded at a density of 5×10^3 cells/well in 96-well flat-bottomed plates for 1 day. Cells were washed twice with PBS and incubated with various concentrations $CaCO_3$-MNPs, free DOX, and DOX-$CaCO_3$-MNPs for 24 h at 37 °C. The cells were washed twice with PBS to eliminate the remaining drugs, and the medium was replaced with cell counting kit-8 solutions (Dojindo Laboratories, Kumamoto). The absorbance of individual wells was measured at 450 nm by a microplate reader (Biorad Elizer, PA). The data are expressed as the percentages of viable cells compared to the survival of a control group. The IC_{50} value was calculated as the concentration of DOX, yielding 50% inhibition of cell proliferation compared to the untreated control.

Monitoring of Cellular Uptake and Intracellular Distribution of FITC-Incorporated DOX-$CaCO_3$-MNPs. To monitor the cellular uptake of

DOX-$CaCO_3$-MNPs, green fluorescent FITC was incorporated into the DOX-$CaCO_3$-MNPs. FITC was labeled on the primary amine terminal of PEG-PAsp block copolymers as follows: To a stirred aqueous solution (pH 7.4) of PEG-PAsp (400 mg, 0.04 mml) was added an aqueous solution (pH 7.4) of FITC (0.8 mg, 0.002 mmol). After being stirred for 24 h at room temperature in the dark, the reaction mixture was dialyzed using a membrane bag (MWCO: 1000 g/mol) to remove the unreacted FITC, followed by lyophilization. The labeling ratio of FITC to PEG-PAsp was estimated by a standard calibration curve and was found to be 2.0%. FITC-incorporated DOX-$CaCO_3$-MNPs was prepared following the identical procedure used for DOX-$CaCO_3$-MNPs, except for using FITC-labeled PEG-PAsp. To monitor cellular uptake, SCC-7 cells (2×10^4 cells/mL per well) were seeded onto a covered glass-bottom dish (SPL Life Sciences) in 2 mL of DMEM supplemented with 10% FBS and 1% antibiotics. After incubation for 24 h (37 °C, 5% CO_2), the medium was carefully aspirated and replaced with 1 mL of medium containing 5 μg/mL DOX equivalent of FITC-incorporated DOX-$CaCO_3$-MNPs. The cells were incubated for 1 and 6 h and washed three times with PBS. The CLSM images of SCC-7 cells treated with FITC-incorporated DOX-$CaCO_3$-MNPs were obtained using a confocal laser scanning microscope.

Visualization of Dissolved Calcium from DOX-$CaCO_3$-MNPs in SCC-7 Cells. SCC-7 cells (2×10^4 cells per well) were seeded onto a covered glass-bottom dish (SPL Life Sciences) in 2 mL of phenol red-free DMEM cell culture medium supplemented with 10% FBS and 1% antibiotics and incubated for 24 h. Rhod-2/AM (50 μg) was dissolved in DMSO (20 μL) and was added to 6.7 mL of phenol red-free DMEM cell culture medium before usage. The Rhod-2/AM solution (2 mL, 6.6 mM) was added to the cell culture chamber and incubated for 30 min. After being washed by PBS three times, the cells were incubated in 1 mL of phenol red-free DMEM cell culture medium containing 100 or 300 μg $CaCO_3$-MNPs for 6 h. After being washed by PBS three times, the cells were fixed with 3.7% formaldehyde for 5 min. Finally, the cells were washed three times with PBS, and then the fluorescence images of Rhod-2-labeled SCC-7 cells treated with $CaCO_3$-MNPs were obtained using a fluorescence microscopy (λ_{ex} = 550 nm, λ_{em} = 580 nm, IX71, Olympus, Japan).

Intracellular Distribution of DOX-$CaCO_3$-MNPs. SCC-7 cells (2×10^4 cells/mL per well) were seeded onto a covered glass-bottom dish (SPL Life Sciences) in 2 mL of DMEM supplemented with 10% FBS and 1% antibiotics (penicillin 100 U/mM, streptomycin 0.1 mg/mL). After incubation for 24 h (37 °C, 5% CO_2), the medium was carefully aspirated and replaced with 1 mL of medium containing 5 μg/mL DOX equivalent of DOX-$CaCO_3$-MNPs and LysoTracker (50 nM). The cells were incubated for 1 and 6 h and then washed three times with PBS. The CLSM images of LysoTracker-labeled SCC-7 cells treated with DOX-$CaCO_3$-MNPs were obtained using a confocal laser scanning microscope (C1si, Nikon, Japan) by green fluorescing (λ_{ex} = 470−490 nm) and red fluorescing (λ_{ex} = 520−550 nm).

Antitumor Effect of DOX-$CaCO_3$-MNPs on SCC-7 Tumor Xenografts. Athymic C3H/HeN nude mice (20−25 g, Harlan, Indianapolis, IN) were used for animal experiments. The tumor model was established by subcutaneously inoculating 1.0×10^6 SCC-7 cells into the left back of a mouse. When tumors grew to approximately 200−250 mm^3, saline (the control group, n = 4), $CaCO_3$-MNPs (the control group, n = 4), free DOX at 10 mg/kg (n = 4), and DOX-$CaCO_3$-MNPs at 10 mg/kg of DOX (n = 4) were administered by a single intratumoral injection. Tumor volumes were calculated as $a \times b^2/2$, where a and b are the largest and smallest diameter, respectively.[43] The statistical analysis was performed using an one-way ANOVA + Tukey's post hoc test.

***In Vivo* Imaging of DOX Clearance Pattern of DOX-$CaCO_3$-MNPs.** All animal treatments and surgical procedures followed approved protocols and were performed in accordance with an NIH-approved protocol. The SCC-7 xenograft tumor was grown in female athymic C3H/HeN nude mice (20−25 g, Harlan, Indianapolis, IN) by inoculating 1.0×10^6 SCC-7 cells into in the right flank side of mice. When tumors reached a size between 250 and 300 mm^3 in volume, 100 μL of PBS solution (pH 7.4) containing free DOX (500 μg/mL, 2 mg/kg of DOX equivalent) or DOX-$CaCO_3$-MNPs (2 mg/kg of DOX equivalent) was administered by an intratumoral injection. The tumor was monitored by using a Maestro all-optical imaging system (Cambridge Research & Instrumentation, Woburn, MA) using blue filter set as the excitation at predetermined time points (immediately after injection (0 h), 12 h, 0.5, 1, 3, 5, and 8 days). For all imaging procedures, mice were anesthetized with 3−4% isoflurane using a nose-cone manifold and restrained on the imaging stage. After 8 days of imaging, the animals were sacrificed. The tumors were harvested for *ex vivo* imaging. Tumors were quantified by ROI analyses on both *in vivo* and *ex vivo* results using the software provided by the vendor.

Statistical Analysis. The statistical significance of differences between experimental and control groups was determined using an one-way ANOVA followed by Tukey's post hoc test. P value of <0.05 or <0.01 were considered significant, and significant differences are shown by asterisks in the figures.

Conflict of Interest: The authors declare no competing financial interest.

Acknowledgment. This work was supported by the National Research Foundation of Korea (NRF) grant funded by the Korea government (MSIP) (Nos. 2013R1A2A2A01009239 and 2012R1A5A2051388).

Supporting Information Available: Details of synthesis and experimental methods. This material is available free of charge *via* the Internet at http://pubs.acs.org.

REFERENCES AND NOTES

1. Lindner, J. R. Microbubbles in Medical Imaging: Current Applications and Future Directions. *Nat. Rev. Drug Discovery* **2004**, *3*, 527–533.
2. Stewart, V. R.; Sidhu, P. S. New Directions in Ultrasound: Microbubble Contrast. *Br. J. Radiol.* **2006**, *79*, 188–194.
3. Willmann, J. K.; van Bruggen, N.; Dinkelborg, L. M.; Gambhir, S. S. Molecular Imaging in Drug Development. *Nat. Rev. Drug Discovery* **2008**, *7*, 591–607.
4. Qin, S. P.; Caskey, C. F.; Ferrara, K. W. Ultrasound Contrast Microbubbles in Imaging and Therapy: Physical Principles and Engineering. *Phys. Med. Biol.* **2009**, *54*, R27–R57.
5. Ferrara, K.; Pollard, R.; Borden, M. Ultrasound Microbubble Contrast Agents: Fundamentals and Application to Gene and Drug Delivery. *Annu. Rev. Biomed. Eng.* **2007**, *9*, 415–447.
6. Schutt, E. G.; Klein, D. H.; Mattrey, R. M.; Riess, J. G. Injectable Microbubbles as Contrast Agents for Diagnostic Ultrasound Imaging: The Key Role of Perfluorochemicals. *Angew. Chem., Int. Ed.* **2003**, *42*, 3218–3235.
7. Kiessling, F.; Gaetjens, J.; Palmowski, M. Application of Molecular Ultrasound for Imaging Integrin Expression. *Theranostics* **2011**, *1*, 127–134.
8. Hernot, S.; Klibanov, A. L. Microbubbles in Ultrasound-Triggered Drug and Gene Delivery. *Adv. Drug Delivery Rev.* **2008**, *60*, 1153–1166.
9. Sanna, V.; Pintus, G.; Bandiera, P.; Anedda, R.; Punzoni, S.; Sanna, B.; Migaleddu, V.; Uzzau, S.; Sechi, M. Development of Polymeric Microbubbles Targeted to Prostate-Specific Membrane Antigen as Prototype of Novel Ultrasound Contrast Agents. *Mol. Pharmaceutics* **2011**, *8*, 748–757.
10. Willmann, J. K.; Kimura, R. H.; Deshpande, N.; Lutz, A. M.; Cochran, J. R.; Gambhir, S. S. Targeted Contrast-Enhanced Ultrasound Imaging of Tumor Angiogenesis with Contrast Microbubbles Conjugated to Integrin-Binding Knottin Peptides. *J. Nucl. Med.* **2010**, *51*, 433–440.
11. Iagaru, A.; Gambhir, S. S. Imaging Tumor Angiogenesis: The Road to Clinical Utility. *Am. J. Roentgenol.* **2013**, *201*, W183–W191.
12. Wilson, S. R.; Burns, P. N. Microbubble-Enhanced US in Body Imaging: What Role? *Radiology* **2010**, *257*, 24–39.
13. Willmann, J. K.; Paulmurugan, R.; Chen, K.; Gheysens, O.; Rodriguez-Porcel, M.; Lutz, A. M.; Chen, I. Y.; Chen, X.; Gambhir, S. S. US Imaging of Tumor Angiogenesis with Microbubbles Targeted to Vascular Endothelial Growth Factor Receptor Type 2 in Mice. *Radiology* **2008**, *246*, 508–518.

14. Kiessling, F.; Gaetjens, J.; Palmowski, M. Application of Molecular Ultrasound for Imaging Integrin Expression. *Theranostics* **2011**, *1*, 127–134.
15. Bloch, S. H.; Wan, M.; Dayton, P. A.; Ferrara, K. W. Optical Observation of Lipid- and Polymer-Shelled Ultrasound Microbubble Contrast Agents. *Appl. Phys. Lett.* **2004**, *84*, 631–633.
16. Min, H. S.; Kang, E.; Koo, H.; Lee, J.; Kim, K.; Park, R.-W.; Kim, I.-S.; Choi, Y.; Kwon, I. C.; Han, M. Gas-Generating Polymeric Microspheres for Long-Term and Continuous *In Vivo* Ultrasound Imaging. *Biomaterials* **2012**, *33*, 936–944.
17. Kang, E.; Min, H. S.; Lee, J.; Han, M. H.; Ahn, H. J.; Yoon, I. C.; Choi, K.; Kim, K.; Park, K.; Kwon, I. C. Nanobubbles from Gas-Generating Polymeric Nanoparticles: Ultrasound Imaging of Living Subjects. *Angew. Chem., Int. Ed.* **2010**, *49*, 524–528.
18. Janib, S. M.; Moses, A. S.; MacKay, J. A. Imaging and Drug Delivery Using Theranostic Nanoparticles. *Adv. Drug Delivery Rev.* **2010**, *62*, 1052–1063.
19. Tassa, C.; Shaw, S. Y.; Weissleder, R. Dextran-Coated Iron Oxide Nanoparticles: A Versatile Platform for Targeted Molecular Imaging, Molecular Diagnostics, and Therapy. *Acc. Chem. Res.* **2011**, *44*, 842–852.
20. Ambrogio, M. W.; Thomas, C. R.; Zhao, Y.-L.; Zink, J. I.; Stoddart, J. F. Mechanized Silica Nanoparticles: A New Frontier in Theranostic Nanomedicine. *Acc. Chem. Res.* **2011**, *44*, 903–913.
21. Melancon, M. P.; Zhou, M.; Li, C. Cancer Theranostics with Near-Infrared Light-Activatable Multimodal Nanoparticles. *Acc. Chem. Res.* **2011**, *44*, 947–956.
22. Pan, D.; Caruthers, S. D.; Hu, G.; Senpan, A.; Scott, M. J.; Gaffney, P. J.; Wickline, S. A.; Lanza, G. M. Ligand-Directed Nanobialys as Theranostic Agent for Drug Delivery and Manganese-Based Magnetic Resonance Imaging of Vascular Targets. *J. Am. Chem. Soc.* **2008**, *130*, 9186–9187.
23. Taratula, O.; Schumann, C.; Naleway, M. A.; Pang, A. J.; Chon, K. J.; Taratula, O. A Multifunctional Theranostic Platform Based on Phthalocyanine-Loaded Dendrimer for Image-Guided Drug Delivery and Photodynamic Therapy. *Mol. Pharmaceutics* **2013**, *10*, 3946–3958.
24. Xiao, Y.; Hong, H.; Matson, V. Z.; Javadi, A.; Xu, W.; Yang, Y.; Zhang, Y.; Engle, J. W.; Nickles, R. J.; Cai, W. Gold Nanorods Conjugated with Doxorubicin and cRGD for Combined Anticancer Drug Delivery and PET Imaging. *Theranostics* **2012**, *2*, 757–768.
25. Yoo, D.; Lee, J.-H.; Shin, T.-H.; Cheon, J. Theranostic Magnetic Nanoparticles. *Acc. Chem. Res.* **2011**, *44*, 863–874.
26. Kim, D.; Jeong, Y. Y.; Jon, S. A Drug-Loaded Aptamer–Gold Nanoparticle Bioconjugate for Combined CT Imaging and Therapy of Prostate Cancer. *ACS Nano* **2010**, *4*, 3689–3696.
27. Choi, K. Y.; Jeon, E. J.; Yoon, H. Y.; Lee, B. S.; Na, J. H.; Min, K. H.; Kim, S. Y.; Myung, S. J.; Lee, S.; Chen, X.; et al. Theranostic Nanoparticles Based on PEGylated Hyaluronic Acid for the Diagnosis, Therapy and Monitoring of Colon Cancer. *Biomaterials* **2012**, *33*, 6186–6193.
28. Gerweck, L. E.; Seetharaman, K. Cellular pH Gradient in Tumor *versus* Normal Tissue: Potential Exploitation for the Treatment of Cancer. *Cancer Res.* **1996**, *56*, 1194–1198.
29. Min, K. H.; Kim, J. H.; Bae, S. M.; Shin, H.; Kim, M. S.; Park, S.; Lee, H.; Park, R. W.; Kim, I. S.; Kim, K.; et al. Tumoral Acidic pH-Responsive MPEG-Poly(β-amino ester) Polymeric Micelles for Cancer Targeting Therapy. *J. Controlled Release* **2010**, *144*, 259–266.
30. Lee, H. J.; Kim, S. E.; Kwon, I. K.; Park, C.; Kim, C.; Yang, J.; Lee, S. C. Spatially Mineralized Self-Assembled Polymeric Nanocarriers with Enhanced Robustness and Controlled Drug-Releasing Property. *Chem. Commun.* **2010**, *46*, 377–379.
31. Min, K. H.; Lee, H. J.; Kim, K.; Kwon, I. C.; Jeong, S. Y.; Lee, S. C. The Tumor Accumulation and Therapeutic Efficacy of Doxorubicin Carried in Calcium Phosphate-Reinforced Polymer Nanoparticles. *Biomaterials* **2012**, *33*, 5788–5797.
32. Rim, H. P.; Min, K. H.; Lee, H. J.; Jeong, S. Y.; Lee, S. C. pH-Tunable Calcium Phosphate Covered Mesoporous Silica Nanocontainers for Intracellular Controlled Release of Guest Drugs. *Angew. Chem., Int. Ed.* **2011**, *50*, 8853–8857.
33. Choi, B.; Park, H.; Hwang, S.; Park, J. Preparation of Alginate Beads for Floating Drug Delivery: Effects of CO_2 Gas Forming Agents. *Int. J. Pharm.* **2002**, *239*, 81–91.
34. Naka, K.; Tanaka, Y.; Chujo, Y. Effect of Anionic Starburst Dendrimers on the Crystallization of $CaCO_3$ in Aqueous Solution: Size Control of Spherical Vaterite Particles. *Langmuir* **2002**, *18*, 3655–3658.
35. Goss, S. L.; Lemons, K. A.; Kerstetter, J. E.; Bogner, R. H. Determination of Calcium Salt Solubility with Changes in pH and P(CO(2)), Simulating Varying Gastrointestinal Environments. *J. Pharm. Pharmacol.* **2007**, *59*, 1485–1492.
36. Wike-Hooley, J. L.; Haveman, J.; Reinhold, J. S. The Relevance of Tumour pH to the Treatment of Malignant Disease. *Radiother. Oncol.* **1984**, *2*, 343–366.
37. Nido, P. J. D.; Glynn, P.; Buenaventura, P.; Salama, G.; Koretsky, A. P. Fluorescence Measurement of Calcium Transients in Perfused Rabbit Heart Using Rhod 2. *Am. J. Physiol.* **1998**, *274*, 728–741.
38. Fonteriz, R. I.; Fuente, S. D. I.; Moreno, A.; Lobaton, C. D.; Montero, M.; Alvarez, J. Monitoring Mitochondrial [Ca2+] Dynamics with Rhod-2, Ratiometric Pericam and Aequorin. *Cell Calcium* **2010**, *48*, 61–69.
39. Daly, W. H.; Poché, D. The Preparation of *N*-Carboxyanhydrides of α-Amino Acids Using Bis(trichloromethyl)-carbonate. *Tetrahedron Lett.* **1988**, *29*, 5859–5862.
40. Lee, S. J.; Min, K. H.; Lee, H. J.; Koo, A. N.; Rim, H. P.; Jeon, B. J.; Jeong, S. Y.; Heo, J. S.; Lee, S. C. Ketal Cross-Linked Poly(ethylene glycol)-Poly(amino acid)s Copolymer Micelles for Efficient Intracellular Delivery of Doxorubicin. *Biomacromolecules* **2011**, *12*, 1224–1233.
41. Harada, A.; Kataoka, K. Novel Polyion Complex Micelles Entrapping Enzyme Molecules in the Core: Preparation of Narrowly-Distributed Micelles from Lysozyme and Poly(ethylene glycol)–Poly(aspartic acid) Block Copolymer in Aqueous Medium. *Macromolecules* **1998**, *31*, 288–294.
42. Decano, J. L.; Moran, A. M.; Ruiz-Opazo, N.; Herrera, V. L. Molecular Imaging of Vasa Vasorum Neovascularization *via* DEspR-Targeted Contrast-Enhanced Ultrasound Microimaging in Transgenic Atherosclerosis Rat Model. *Mol. Imaging Biol.* **2011**, *13*, 1096–1106.
43. Min, K. H.; Park, K.; Kim, Y.-S.; Bae, S. M.; Lee, S.; Jo, H. G.; Park, R.-W.; Kim, I.-S.; Jeong, S. Y.; Kim, K.; et al. Hydrophobically Modified Glycol Chitosan Nanoparticles-Encapsulated Camptothecin Enhance the Drug Stability and Tumor Targeting in Cancer Therapy. *J. Controlled Release* **2008**, *127*, 208–218.